Original Article

Repeated Iron–Soot Exposure and Nose-to-brain Transport of Inhaled Ultrafine Particles

Laurie E. Hopkins[1], Emilia A. Laing[1], Janice L. Peake[1], Dale Uyeminami[1], Savannah M. Mack[1], Xueting Li[1,2], Suzette Smiley-Jewell[1], and Kent E. Pinkerton[1]

Abstract

Particulate exposure has been implicated in the development of a number of neurological maladies such as multiple sclerosis, amyotrophic lateral sclerosis, Alzheimer's disease, and idiopathic Parkinson's disease. Only a few studies have focused on the olfactory pathway as a portal through which combustion-generated particles may enter the brain. The primary objective of this study was to define the deposition, uptake, and transport of inhaled ultrafine iron–soot particles in the nasal cavities of mice to determine whether combustion-generated nanoparticles reach the olfactory bulb via the olfactory epithelium and nerve fascicles. Adult female C57B6 mice were exposed to iron–soot combustion particles at a concentration of 200 $\mu g/m^3$, which included 40 $\mu g/m^3$ of iron oxide nanoparticles. Mice were exposed for 6 hr/day, 5 days/week for 5 consecutive weeks (25 total exposure days). Our findings visually demonstrate that inhaled ultrafine iron–soot reached the brain via the olfactory nerves and was associated with indicators of neural inflammation.

There is a well-established association between exposure to particulate matter (PM) and numerous adverse cardiopulmonary health effects. Inhaled PM can readily cross the air-to-blood tissue barrier of the lungs with higher efficiency of systemic distribution as particle size decreases (Kreyling et al. 2002). Particulate exposure has been implicated in the possible development of neurological conditions such as Alzheimer's and idiopathic Parkinson's disease (Gotz et al. 2004; Kovacs 2004; Linse et al. 2007). Although extensive efforts have been directed toward understanding particle fate and cell–particle interactions in pulmonary and cardiovascular targets, those mechanisms and pathways through which inhaled PM may act on the central nervous system are just now becoming more fully explored. PM may have enhanced entry to the brain from the systemic circulation by crossing the blood-to-brain endothelial barrier, perhaps via exposure-related changes in endothelial membrane permeability. Another possibility is PM may bypass the blood–brain barrier by entering the brain directly via uptake by olfactory sensory neurons (OSNs), which have a direct connection to the olfactory epithelial lining of the nasal cavity with extension of their axons directly to the region of the olfactory bulb of the brain (Mombaerts 2006).

Ambient particulates in polluted air can consist of a multifaceted mixture of highly diverse chemical entities, including hydrocarbons, sulfates, nitrates, metals, soot, and a combination of other organic and inorganic compounds (Kumar and Gill 2009; Ngo et al. 2010). Combustion-derived PM commonly contains transition metals, with iron being the predominant metal found in the ultrafine size fraction (Hughes and Cass 1998). A leading hypothesis contends that exposure to transition metals, such as iron, elicits a pro-inflammatory response through redox cycling that is initially localized to sites of particle deposition but may lead to a subsequent generalized inflammatory condition should the stimulus be sufficiently robust or persistent. If clearance of inhaled PM or nanoparticles is delayed, a chronic inflammatory condition could result. Such inflammatory processes of the brain are thought to play a central role in neurological dysfunction and disease (Cameron and

[1] Center for Health and the Environment, University of California, Davis, Davis, California, USA
[2] Institute of Human Nutrition, Columbia University, New York, New York, USA

Corresponding Author:
Kent E. Pinkerton, Center for Health and the Environment, University of California, Davis, Davis, California 95616, USA.
Email: kepinkerton@ucdavis.edu

Landreth 2010; Chakraborty et al. 2010; Czlonkowska and Kurkowska-Jastrzebska 2011; Kim and Joh 2006; Majde 2010; Pott Godoy et al. 2008).

The primary objective of this study was to define and visualize the uptake and transport of iron particles in the olfactory pathway. A secondary objective was to determine whether the presence of iron–soot particles in the olfactory bulb would provoke an inflammatory response. To accomplish these goals, an iron–soot combustion particle aerosol was experimentally generated at a concentration of 200 μg/m³, including 40 μg/m³ of iron nanoparticles, using a laminar diffusion flame system (Yang et al. 2001). Exposure of mice to this aerosol took place for 6 hr/day, 5 days/week for a total of 5 weeks (25 exposure days).

Materials and Methods

Animals

Thirty-six adult female C57B6 mice (23 $\pm$ 1.2 g body weight) 9 weeks of age at the onset of experimental exposure were purchased from Charles River Labs (Wilmington, MA). Mice were randomly assigned to 2 exposure groups (iron–soot, $n = 24$; filtered air, $n = 12$) and allowed to acclimate for at least 1 week prior to the onset of experimental exposures. Mice were housed, up to 4 per cage, in filter-top polycarbonate cages in an animal facility with high-efficiency particulate air filters. Except during the actual period of exposure, mice were given access to water and a standard laboratory mouse diet *ad libitum*. All animals were handled in accordance with guidelines established by the Institutional Animal Care and Use Committee of the University of California, Davis.

Inhalation Exposures

Mice were housed in sealed 20 cm $\times$ 43 cm $\times$ 18 cm polycarbonate whole-body chambers during exposure to an aerosol of ultrafine iron–soot at a target concentration of 200 μg/m³, including 40 μg/m³ of iron oxide nanoparticles. The total soot–iron aerosol generated was cooled and diluted with filtered air to achieve the desired concentration prior to reaching the exposure chambers. Mice were exposed 6 hr/day, 5 days/week for 5 consecutive weeks (25 total exposure days). The sham control group was exposed to filtered air only. Flow rate through the whole-body exposure chambers was 7 L/min for a total air exchange of 2.2/min or 133/hr. Chamber ozone and CO_2 levels were not detected, while oxides of nitrogen were below 0.1 ppm. Chamber temperature averaged 68 to 70°F. During each exposure period, the animals were unrestrained and allowed to engage in normal activity, although access to food and water was denied.

Generation and Characterization of Particles

Particles were generated in a laminar diffusion flame system using ethylene gas as the primary hydrocarbon fuel mixed with acetylene gas to compensate for the effect of iron oxide to suppress soot formation (Figure 1). The source of iron was iron pentacarbonyl vaporized from a liquid reservoir warmed to 20°C with an argon carrier gas (all Sigma-Aldrich Chemical Co., St. Louis, MO) combusted in the presence of an ethylene/acetylene vapor mix. Combustion of these reactants generated a heterodisperse aerosol of ultrafine iron oxide particles (Fe_2O_3) and associated soot. A detailed description of the system and the particles generated is available (Jasinski et al. 2006; Pinkerton et al. 2008; Yang et al. 2001). A target particle concentration of 200 μg/m³ was selected to simulate unhealthy air quality conditions, while remaining at a concentration of particulate emissions that would be reminiscent of heavy pollution days seen with wildfires in the United States in recent years, as well as poor air quality days experienced today in many parts of the world including China (Pui, Chen, and Zuo 2014; Connor 2015). Aerosol was collected daily on 25 mm Teflon-coated filters (Teflo Pall, East Hills, NY) of 3.0 mm pore size and sent to an independent laboratory (Chester Labnet, Tigard, OR) for metal analysis by X-ray fluorescence to determine iron content. Total mass concentration data were obtained gravimetrically by weighing 25 mm Pallflex Emfab filters (VWR International, Radnor, PA) on a microbalance before and after sample collection. Samples for transmission electron micrograph particle visualization were collected on 3 mm carbon-coated ("lacey carbon") copper grids using a point-to-plane electrostatic precipitator (Figure 2). A scanning mobility size analyzer (scanning mobility particle sizer [SMPS] 3936, TSI, Shoreview, MN) was run concurrently during animal exposure to determine particle size distribution. These data were collected to determine whether the desired size and target concentration were achieved and to provide a measure of uniformity of exposure during the course of the experiment (Figure 3).

Tissue Collection

Twenty-four hours following the final exposure day, mice were deeply anesthetized by an intraperitoneal injection of sodium pentobarbital anesthetic (65 mg/g body weight; Nembutal, Cardinal Health, Sacramento, CA) diluted 1:6 with phosphate-buffered saline solution at 1 mg/kg body weight, for example, 0.03 cc for a 30 g mouse. A total of 32 mice were used for histological and protein analysis (12 control and 20 exposed).

Fixed tissue: Nasal cavity, olfactory bulb, and brain. When complete sedation was achieved (i.e., the mouse was unresponsive to toe pinch test), the thorax was opened and the lungs inflated to 18 psi via cannulation of the trachea. Whole-body fixation was achieved by vascular perfusion with heparinized phosphate-buffered saline (United States Pharmacopeia grade) followed by 4% paraformaldehyde. The cannula for perfusion was placed into the right ventricular chamber with flow directed toward the pulmonary valve and trunk and outflow through the jugular vein. Perfusion-fixed tissues were harvested and immersed in 4% paraformaldehyde until further processing for histological analyses. The cranium was opened along the dorsal midline to remove the brain olfactory bulb, taking care to
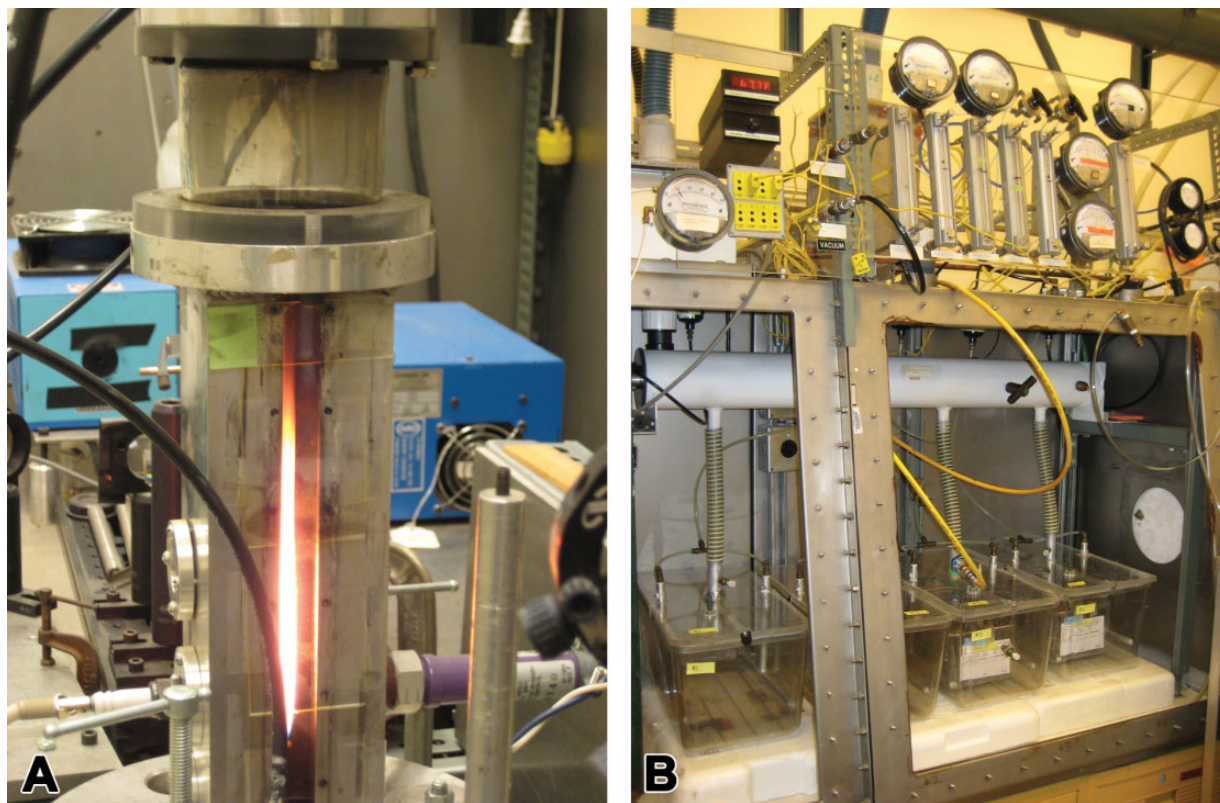
Figure 1. (A) Laminar diffusion flame system used to generate ultrafine iron oxide and soot particles. (B) Whole-body exposure chambers designed to deliver a constant stable concentration of total iron–soot combustion particles for 6 hr/day, 5 days/week for a total of 5 weeks.

minimize stretching of the olfactory nerves. Nasal cavities were gently flushed in a retrograde manner with fixative using a syringe inserted into the exposed end of the trachea. Retrograde perfusion was done to ensure that fixative exited both nares, indicating complete flushing of the nasal cavity. The lower jaw was removed, and the head cleaned of skin and superficial muscles. Trimmed heads were immersed in fixative for at least 24 hr prior to demineralization in 10% ethylenediaminetetraacetic acid (EDTA) solution (Immunocal, American MasterTech, Lodi, CA), followed by further trimming, slicing of the nasal cavity, and eventual embedment in Paraplast (Fisher Scientific, Swedesboro, NJ).

Unfixed tissue: Olfactory bulb and brain. Mice were killed by decapitation using a guillotine after complete sedation (verified by toe pinch test), and the brain was immediately removed in the manner described above. Olfactory bulbs were processed and analyzed separately from other portions of the brain. Homogenates of the olfactory bulb were prepared for protein analysis.

Histologic Preparation of the Nasal Cavity, Olfactory Bulb, and Brain—Staining Methodology

When preparing and cutting the nasal cavity, olfactory bulb, and brain for embedment in Paraplast, care was taken to avoid particle transfer; each cut was made with a fresh blade in a caudal-to-rostral direction. Sagittal sections of nasal cavities were cut using a microtome to a thickness of 5 μm, while the brain and olfactory bulb tissues were serially sectioned to 10 μm. Within the nasal cavity, step series at 50 μm intervals were taken for identification of the olfactory epithelium and nerve bundles within the nasal cavity along with the localization of ferric iron within neural and olfactory tissues. Microglial cells within the olfactory bulb were visualized using Ricinus communis agglutinin (RCA-1) lectin, which strongly binds to microglial cells to categorize both resting and activated forms of the cell (Wierzba-Bobrowicz, Lechowicz, and Kosno-Kruszewska 1997).

Ferric Iron Visualization

Iron was visualized directly in fixed, paraffin embedded sections of nasal cavity, brain, and olfactory bulb by staining with Prussian blue, a standard histologic method of detecting iron in tissue in which ferric iron interacts with potassium ferrocyanide to form ferric ferrocyanide, a deep blue precipitate. Only the insoluble form of iron, ferric iron (Fe^{+++}), is labeled by this technique. Neutral red was used as a counterstain to visualize nuclei and to lightly stain surrounding structures. A complete series of step sections of the olfactory bulb at 50 μm intervals was collected.
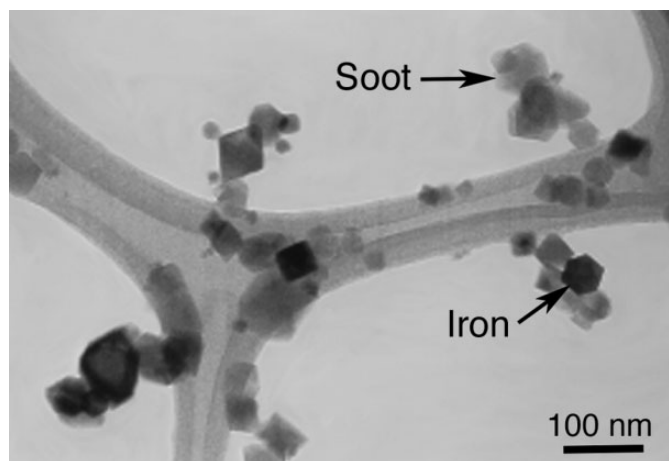
Figure 2. Transmission electron micrograph of iron–soot particles collected on a carbon-coated holey grid.
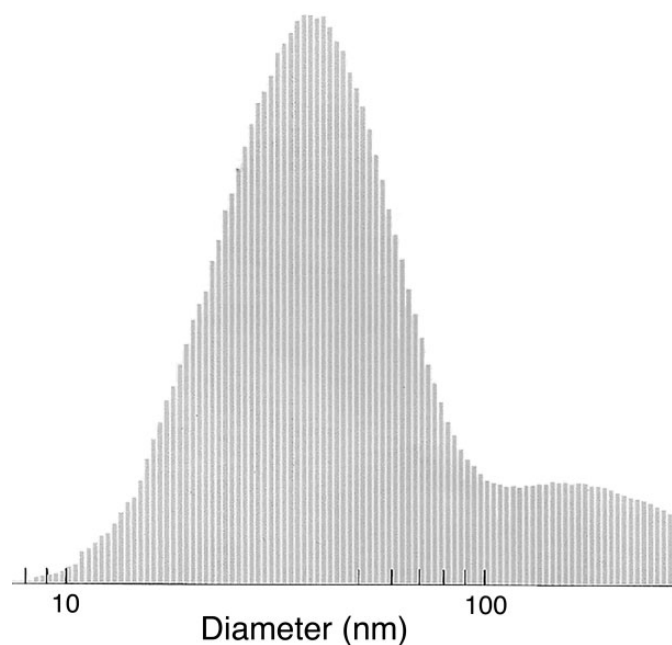

Figure 3. Histogram of nanoparticle size as measured by a scanning mobility particle sizer with a mean particle size of 50 ± 4 nm.

Olfactory and Microglial Cell Visualization

Staining with hematoxylin and eosin (H&E) was used to visualize the anatomy and composition of the nasal cavity, olfactory bulb, and brain. Sections of the nasal cavity were also stained with protein gene product 9.5 (PGP9.5), a general nerve marker (Pinkerton and Joad 2006) antibody specific for olfactory epithelium, nerves, and nerve fascicles. Microglial cells in sections of the olfactory bulb tissue were visualized using RCA-1 staining (Vector Labs, Burlingame, CA) as per a modified method of Hauke and Korr (1993). Briefly, tissue sections were deparaffinized, incubated with RCA-1 lectin followed by

3,3′-diaminobenzidine chromogen + substrate (Dako North America, Carpinteria, CA) and counterstained with hematoxylin. Antigen retrieval using hydrogen peroxide was implemented to increase binding sites to achieve strong, specific labeling with low background and adequate contrast to view cell morphology in 10-μm thick sections.

RCA-1 binds to β-D-galactose moieties present on microglial cells, epithelial cells, and vascular endothelial cells, which are easily differentiated on the basis of their morphology. Microglial cells exhibit a range of morphological conformations correlating with activation state, presenting a gradient from resting to fully activated (Colton and Wilcock 2010; Lawson et al. 1990; Stence, Waite, and Dailey 2001). Microglial cells were counted in 2 histological sections per animal for 6 animals per exposure group. All microglial cells were counted in each of 6 nonoverlapping fields per section and classified as either resting or activated using predetermined criteria based on Stence's characterization of ramified versus motile stages (Stence, Waite, and Dailey 2001). Criteria for microglial cell categorization as "resting" included strong RCA-1 lectin-positive staining and at least 2 highly branched (ramified) processes extending at least twice the length of a highly elliptical (flattened) nucleus. Criteria for microglial cell categorization as "activated" included strong RCA-1 lectin-positive staining and no more than 2 visible processes of more than half the length of the large roughly circular nucleus or large overall size and amoeboid shape accompanied by dense staining. RCA-1 positive cells not meeting either set of criteria (i.e., intermediate forms) were excluded from counting. Two levels of the olfactory bulb were analyzed with 6 fields per level using a 20× objective lens for a total of 12 nonoverlapping fields. A total of 6 animals from each group were examined. Activated and resting microglial cells were counted for each animal. The ratio of activated to resting microglial cells was also determined.

Preparation of Tissue Homogenates

Olfactory bulb homogenates were prepared from unfixed frozen tissues placed in flat bottom tubes (Eppendorf North America, Hauppauge, NY) containing stainless steel balls, lysis buffer (Pierce Protein Research, Thermo Fisher Scientific, Waltham, MA), protease inhibitor cocktail (Complete, Roche Diagnostics, Indianapolis, IN), and sonicated for 4 min at 20 Hz in a Qiagen TissueLyser (Qiagen Inc., Valencia, CA). Aliquots were stored on ice until cytokine and total protein content analyses.

BCA Protein Assay

Total protein in olfactory bulb homogenates was determined using a commercially available Bicinchoninic Acid (BCA) protein assay kit (Pierce Protein Research, Rockford, IL) in accordance with the manufacturer's instructions for a 96-well plate micro-assay. Assays were read on a BioTek Synergy2 plate reader with version 3.03 of Gen5 software (BioTek Instruments, Winooski, VT).
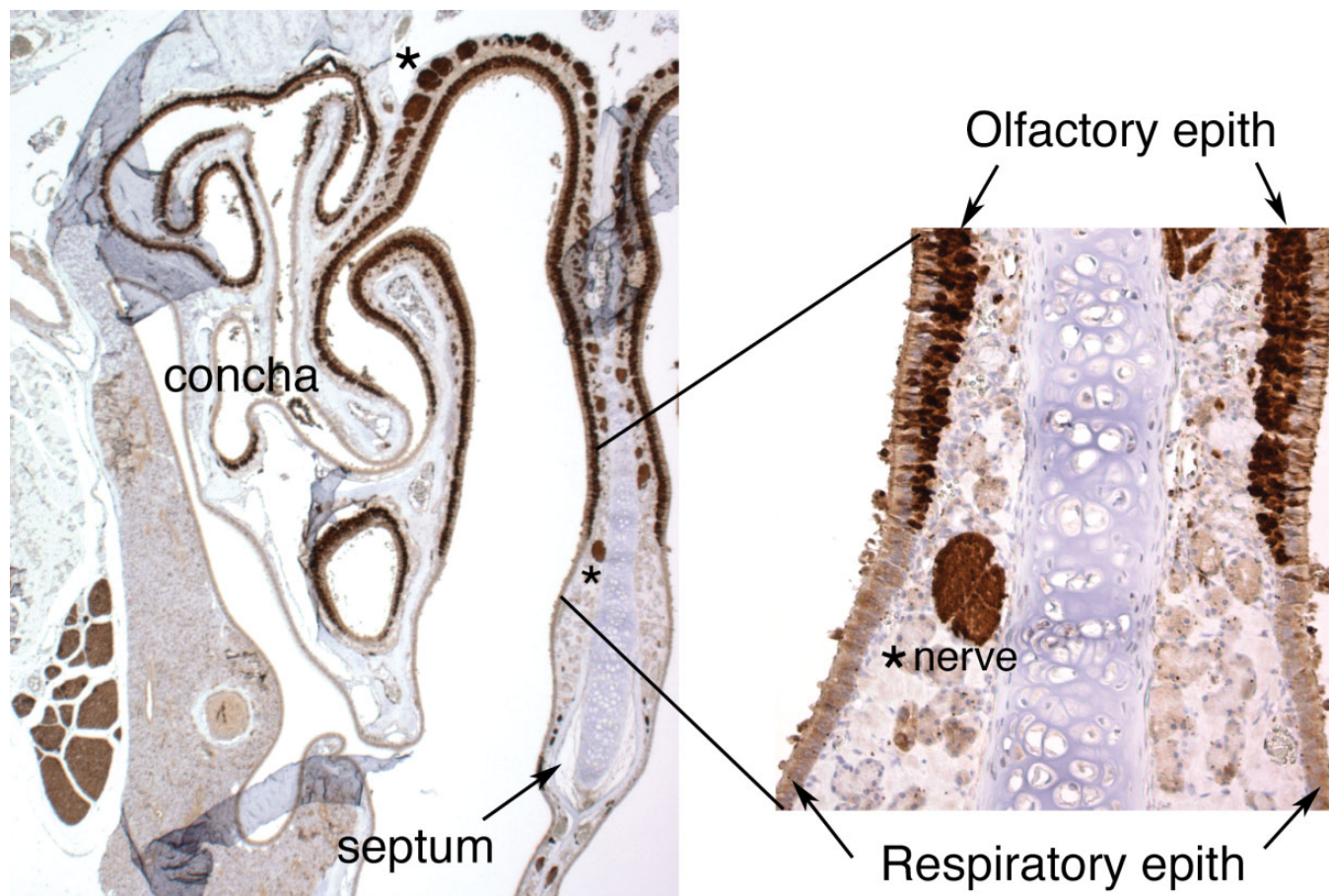
Figure 4. Cross-sectional view of the murine nasal cavity stained with protein gene product 9.5, a general nerve marker, to visualize neural positive tissues and cells, including the olfactory epithelium, nerves, and nerve bundles. The region shown includes the upper portions of the caudal region of the nasal cavity with clearly marked regions of olfactory epithelium and underlying nerves.

ELISA for Cytokines

Levels of the pro-inflammatory cytokines Tissue Necrosis Factor-α (TNF-α) and Interleukin-1β (IL-1β) were analyzed in olfactory bulb homogenates using commercial Enzyme-Linked ImmunoSorbent Assay (ELISA) kits (Cell BioLabs, San Diego, CA; R&D Systems Inc., Minneapolis, MN, respectively). Homogenates were diluted as necessary to achieve the protein concentration recommended by each ELISA kit manufacturer. However, due to the small size of the mouse olfactory bulbs collected, the volume of tissue homogenate available for these assays was limited and precluded the use of a more concentrated sample for analysis of TNF-α on a per mouse basis.

Statistical Analysis

For quantitative end points (cytokine expression and microglial cell counts), mean values per exposure group were determined and expressed $\pm$ standard deviation. Data were analyzed using Excel (Microsoft Corporation, Redmond, WA). Student's t test was performed on group mean values with significance accepted at $p \leq .05$.

Results

Ultrafine Iron–Soot Aerosol Characterization

Particle size distribution remained consistent between samples taken daily during the exposure. Average total suspended particle mass concentration for the 25 exposure days was 203 $\pm$ 13 $\mu g/m^3$, of which an average 38 $\mu g/m^3$ was composed of iron. Daily median particle diameter ranged from 44 nm to 59 nm; the 25-day average was 50.4 $\pm$ 4 nm.

Identification of Olfactory Epithelium and Pathways to the Olfactory Bulb and Brain

PGP9.5 staining of transverse sections through the nasal cavity (Figure 4) demonstrates the extensive distribution of the olfactory epithelium and nerve fascicles throughout the caudal portions of the nasal cavity, in particular in both posterior and apical regions. A sagittally cut tissue section through the posterior region of the nasal cavity stained with H&E (Figure 5) shows in a single plane the relative position of the olfactory epithelium to the nerve fascicles that pass through the cribriform plate to the olfactory bulb (Figure 5). This plane of
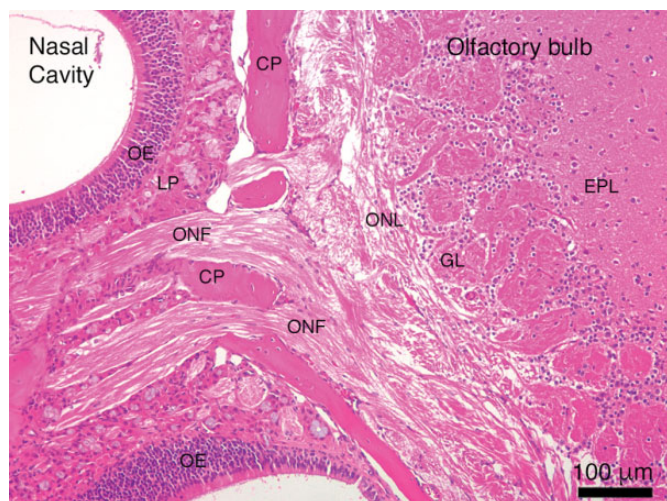
Figure 5. Direct visualization of the neural pathway from the nasal cavity to the olfactory bulb of the brain. CP = cribriform plate; EPL = external plexiform layer; GL = glomerular layer; LP = lamina propria; OE = olfactory epithelium; ONF = olfactory nerve fascicle; ONL = olfactory nerve layer.

section also allows for the visualization of the glomerular and external plexiform layers of the olfactory bulb where the individual olfactory nerve axons synapse with the olfactory bulb (Figure 5).

Visualization of Iron in Olfactory Tissues and Nerves

Prussian blue reaction product, indicative of the presence of ferric iron, was found abundantly in the olfactory nerve fascicles leading to the olfactory bulb of iron–soot combustion particle exposed mice (Figure 6). Prussian blue staining was not noted in the sham-exposed controls (data not shown). Occasional strong punctate iron-positive staining of olfactory nerve fascicles exiting the olfactory epithelium was noted en route to the olfactory bulbs with small foci of iron accumulation within the olfactory bulbs observed (Figure 7). Iron distribution was not completely uniform; only a few of the olfactory nerve fascicles in any given tissue section were iron positive. In addition, it was noted in some nerve fascicles that the iron appeared to be limited to the outer layers of the nerve bundle (Figure 6B). Specific regions of the olfactory bulb in mice exposed to iron–soot were stained iron positive, primarily in the posterior portion of the bulb, near the boundary of the accessory olfactory bulb. Iron-laden cells were also occasionally observed in these posterior regions of the bulb. Iron staining in the apical region of the olfactory epithelium was only occasionally observed and always in a fine punctate manner.

Microglial Cells and Markers of Inflammation in the Olfactory Bulb

Microglial cells and the endothelium/smooth muscle of blood vessels stained positively for RCA-1 lectin (Figure 8). Resting
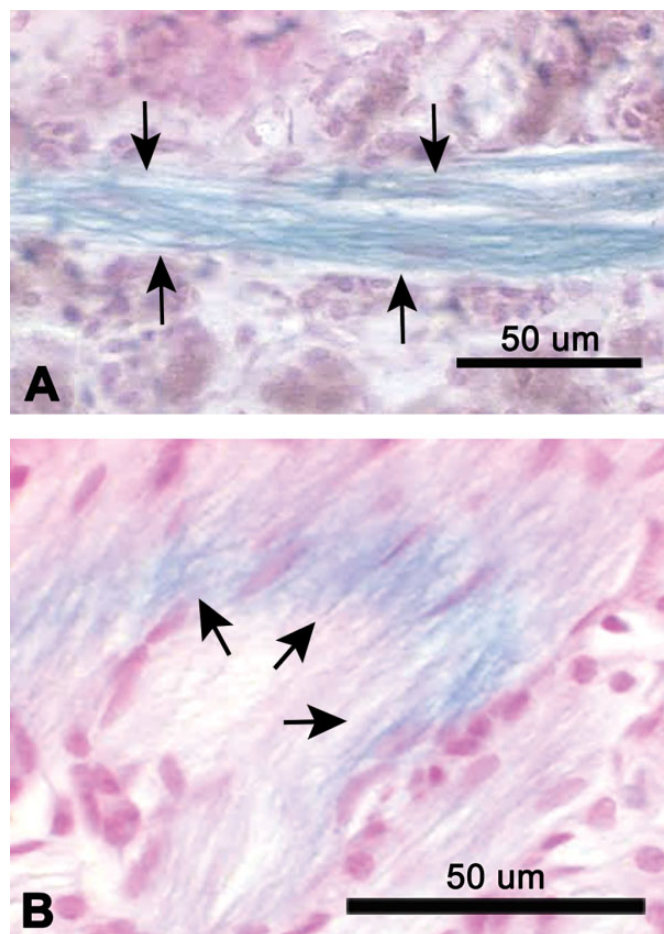

Figure 6. Light micrographs of paraffin sections of nasal cavities from iron–soot exposed mice, showing the lamina propria region of olfactory mucosa. (A) The plane of section is roughly parallel to the fascicle. (B) The plane of section cuts across several nerve fascicles at an oblique angle, producing an elliptical cross section. Arrows indicate Prussian blue-positive olfactory nerve fibers, demonstrating the presence of ferric iron. Tissues are counterstained with neutral red.

microglia were visualized as thin, elongated extensions of cytoplasm between neural cells, while activated microglia possessed short, stubby processes close to the centrally located nucleus.

The total number of microglial cells (activated and resting) per unit area of the olfactory bulb did not significantly change between sham control animals and animals exposed to ultrafine iron–soot particles (Figure 9). In contrast, the ratio of activated to resting microglial cells was significantly greater in mice exposed to iron–soot in contrast to that observed in sham controls (0.47 vs. 0.39; $p = .045$; Figure 10).

The level of the pro-inflammatory cytokine IL-1β in olfactory bulb homogenates from iron–soot-exposed mice was significantly greater compared to IL-1β measured in sham control mice (Figure 11). In contrast, TNF-α levels were near or below the detection limit of the assay in both exposure groups (data not shown).
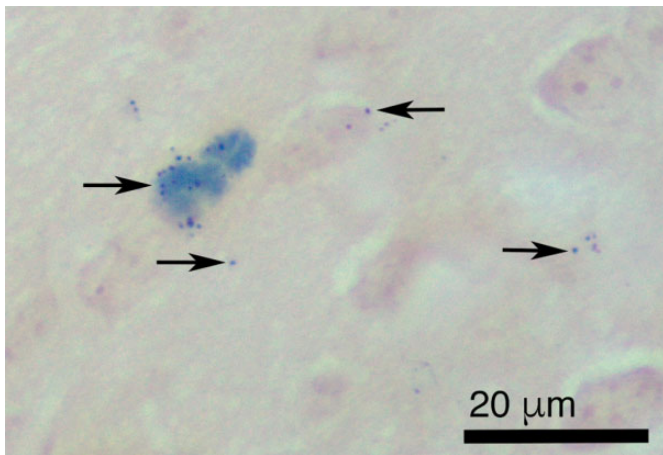
Figure 7. Light micrograph of paraffin section of olfactory bulb from iron–soot exposed mice. Arrows indicate Prussian blue reaction product (deep blue precipitate) demonstrating the presence of ferric iron in the olfactory bulb. Neutral red counterstain.

Discussion

The primary objective of this study was to detect the deposition, uptake, and transport of inhaled ultrafine iron–soot particles via the olfactory pathway to the brain. Although particles may reach the brain via other pathways, nose-to-brain transport of metals has been reported in a limited number of studies. With rare exceptions, the method of exposure in these studies was by intranasal instillation of ionic forms of the particle. More recent studies of nose-to-brain delivery of engineered nanoparticles for therapeutic goals also in general apply intranasal instillation as the preferred method of administration. Recent research further exploring the potential toxic effects of nanoparticles reaching the brain is still developing (Ahmad et al. 2016; Gao 2016; Hao et al. 2016; Muntimadugu et al. 2016), although the actual passage of these particles has not been visualized.

Setting aside the question of how well intranasal delivery of a bolus of particles substitutes for exposure by inhalation to an aerosol, the data presented as evidence of OSN-mediated transport continue to be suggestive, circumstantial, and not absolutely confirmatory (Doty 2008; Mistry, Stolnik, and Illum 2009; Oberdorster et al. 2004; Rao et al. 2003). In these published studies, translocated particles are presumed to have reached the brain by way of olfactory axonal tracts despite the paucity of direct evidence to support the assumption. The current study supplies this evidence by visually demonstrating olfactory nerve uptake of iron using Prussian blue staining.

Although nerve fascicles arising from the olfactory epithelium demonstrated the uptake of iron by way of Prussian blue staining, abundant iron-positive staining within the glomerular layer of the olfactory bulb was not observed in histological sections. In contrast, iron as visualized by Prussian blue staining was found distributed in the deeper layers of the olfactory bulb. This observation might suggest iron found in the
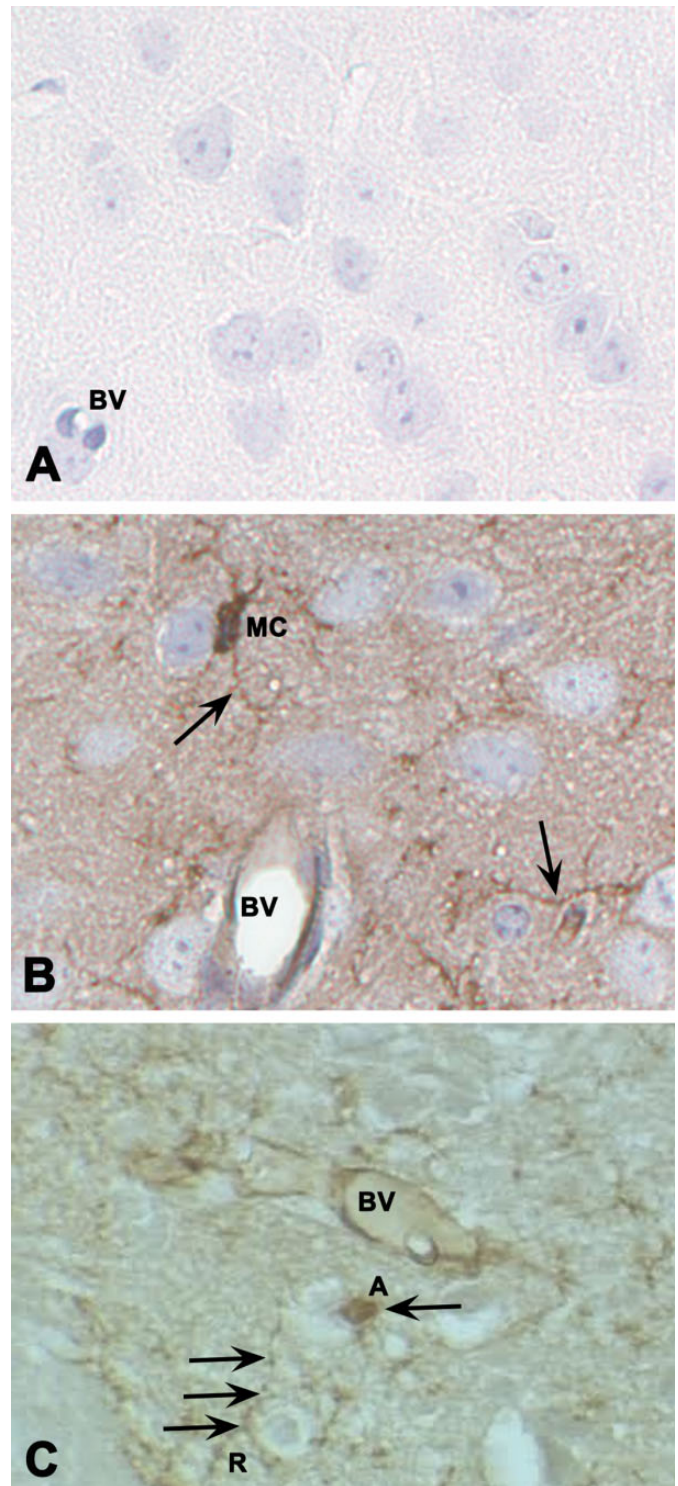

Figure 8. Immunostaining of microglial cells of the olfactory bulb with Ricinus communis agglutinin (RCA-1) lectin. (A) The negative control with primary RCA-1 lectin antibody omitted. (B) Diffuse staining of RCA-1 lectin-positive cells with prominent microglial staining of the cell body (MC) and thin, elongated cytoplasmic processes extending beyond the cell nucleus (arrows). (C) An activated microglial cell (labeled A) exhibited a large, rounded nucleus and retraction of cytoplasmic processes, while resting microglial cells

olfactory bulb could have arrived by way of the systemic circulation. Much of the aerosol in these inhalation exposures reached the lung (data not published). Most particles deposited in pulmonary regions are cleared via the mucociliary escalator and subsequently swallowed. Some bioavailable iron has been identified in the aerosols generated in our combustion particle system (Pinkerton et al. 2008). Thus, it is possible that some iron may have been taken up from the lung or the gut with iron in the blood entering the brain by crossing vascular endothelial membranes.

In general, movement of iron in the body is tightly regulated. However, when inflammation is present, there may be changes in the movement of iron across the blood–brain barrier due to increased vascular permeability (Shaftel et al. 2007; Thornton et al. 2010). Nevertheless, we believe this is not the primary route for entry of iron to the olfactory bulb and brain in this study for several reasons: (1) the pro-inflammatory response observed was not pronounced, (2) there is strong evidence of iron in the olfactory nerve tracts linking the nasal mucosa to the olfactory bulb, and (3) foci of iron accumulation are found in the olfactory bulb but not elsewhere in the brain. A study from our laboratory showed nose-to-brain transport of aerosolized quantum dots, a form of semiconductor nanocrystal, in mice occurred with significant activation of microglial cells (Hopkins et al. 2014). This study, although not comprehensive, demonstrated the presence of quantum dots along axonal pathways by transmission electron microscopy as well as fluorescent detection of quantum dots in unfixed olfactory bulb preparations. Similarly, silver nanoparticles were found transported to the olfactory bulb of rats, also demonstrating microglial cell activation (Patchin et al. 2016). A recent article reviewed a number of papers in the literature in which olfactory nerve transport was observed (Heusinkveld et al. 2016). While we acknowledge there are other pathways through which ultrafine particles may reach the brain, the primary purpose of this study was to verify that ultrafine particles found in combustion emissions can be transported to the brain via the olfactory route.

Although the lung is a primary site for the deposition of inhaled ultrafine particles, there is also a high level of deposition of ultraparticles in the nasal cavity as well. The current study suggests the upper respiratory tract contributes in a different, but significant fashion to total brain uptake, highlighting the potential for multiplicity of particle effects by particles acting on different targets concurrently. Our results demonstrate increased microglial cell activation and neural inflammation. Zhong et al. also noted significant pro-inflammatory responses to the same ultrafine iron–soot material at higher exposure concentrations (Zhong et al. 2010; Zhou, John, Kennedy, Pinkerton, et al. 2003) and at lower concentrations comparable to those used in this study to cause significant synergistic effects of iron–soot exposure (Zhong

Figure 8. (continued). (labeled R) had small, elliptical nuclei and long, branched processes. Hematoxylin counterstain. BV = blood vessel; MC = microglial cells.
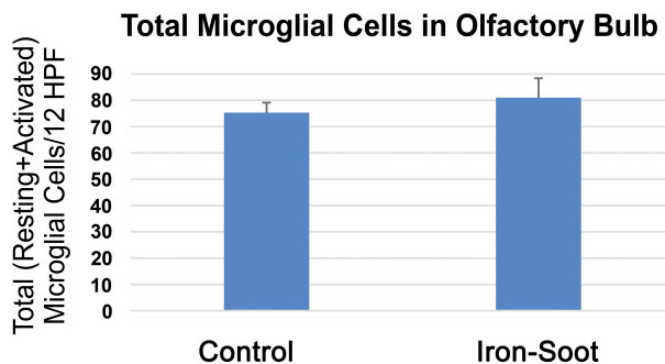
Total Microglial Cells in Olfactory Bulb

Figure 9. Graph of total (resting + activated) microglial cells for sham controls and animals exposed to iron–soot ultrafine particles. Two different levels of the olfactory bulb were analyzed at 20× magnification. Six nonoverlapping high power fields per level were analyzed for a total of 12 nonoverlapping fields. Six animals from each group were examined. Group means were 75.3 ± 9.3 in sham controls and 81 ± 20.8 in animals exposed to iron–soot nanoparticles. No statistical significance was achieved ($p = .25$).
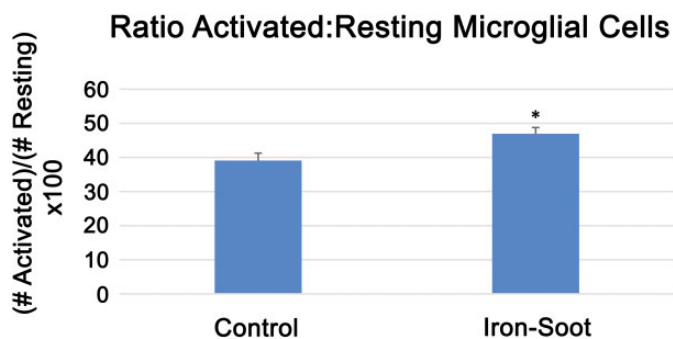
Ratio Activated:Resting Microglial Cells

Figure 10. The ratio of activated to resting microglial cells in the olfactory bulb of sham controls and animals exposed to iron–soot ultrafine particles. The ratio was 0.39 in sham controls and 0.47 in animals exposed to iron–soot ultrafine particles; there was a significant difference between groups (*$p = .045$).
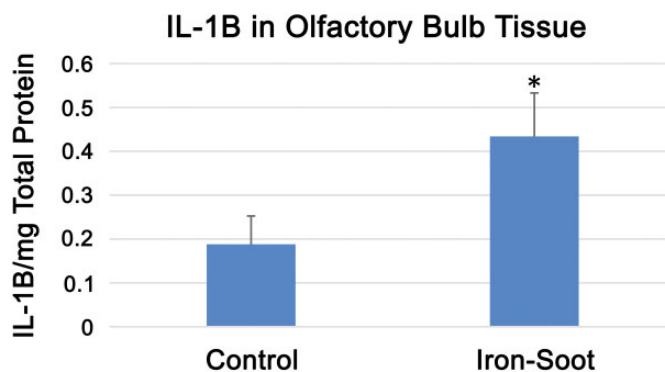
IL-1B in Olfactory Bulb Tissue

Figure 11. IL-1β levels in the olfactory bulb for sham controls and animals exposed to iron–soot ultrafine particles. Group means were 0.19 ± 0.11 pg/mg (control) and 0.43 ± 0.24 pg/mg (iron–soot); a statistically significant difference was noted between groups (*$p = .038$).

et al. 2010; Zhou, John, Kennedy, Leppert, et al. 2003). In this study, we opted not to use higher concentrations of iron to create what we felt would be an environmentally relevant level of metals within our iron–soot combustion particulate emission system delivered to the nose and rest of the respiratory tract via inhalation.

In summary, this study confirms inhaled ultrafine iron oxide can reach the brain via olfactory nerve fascicles. Evidence of inflammatory changes in the olfactory bulb following exposure to ultrafine iron–soot particles provides further support to the concept that long-term exposure to ambient PM may play a role in neurological disease in humans. In addition, as nanoparticles continue to be developed to treat neurological diseases, it is important to take into consideration possible pro-inflammatory changes in the central nervous system (CNS) that these particles could elicit. The combined effect of concurrent particle-related responses in multiple targets, such as the lung and the olfactory bulb, could lead to a generalized adverse impact on the health of susceptible individuals. It may be the case that long-term exposure to low levels of ultrafine PM results in a chronic inflammatory state, a condition associated with chronic disease in humans. As speculation that exposure to airborne particles might be a causative agent in neurodegenerative disorders continues to grow, further investigation of the olfactory pathway as a port of entry is warranted.

Authors' Note

Laurie E. Hopkins and Emilia A. Laing contributed equally to this research.

Acknowledgments

Author Contribution

All authors (LH, EL, JP, DU, SM, XL, SS, and KP) contributed to conception or design; data acquisition, analysis, or interpretation; drafting the manuscript; and critically revising the manuscript. All authors gave final approval and agreed to be accountable for all aspects of work in ensuring that questions relating to the accuracy or integrity of any part of the work are appropriately investigated and resolved.

Declaration of Conflicting Interests

The author(s) declared no potential conflicts of interest with respect to the research, authorship, and/or publication of this article.

Funding

ORCID iD

Kent E. Pinkerton 🔟 http://orcid.org/0000-0001-6868-7572

References

Ahmad, N., Ahmad, R., Naqvi, A. A., Alam, M. A., Ashafaq, M., Samim, M., Iqbal, Z., Ahmad, F. J., et al (2016). Rutin-encapsulated chitosan nanoparticles targeted to the brain in the treatment of Cerebral Ischemia. *Int J Biol Macromol* **91**, 640–55.

Cameron, B., and Landreth, G. E. (2010). Inflammation, microglia, and Alzheimer's disease. *Neurobiol Dis* **37**, 503–09.

Chakraborty, S., Kaushik, D. K., Gupta, M., and Basu, A. (2010). Inflammasome signaling at the heart of central nervous system pathology. *J Neurosci Res* **88**, 1615–31.

Colton, C., and Wilcock, D. M. (2010). Assessing activation states in microglia. *CNS Neurol Disord Drug Targets* **9**, 174–91.

Connor, N. (2015). Choking smog more than 50 times health guidelines blankets China. *The Telegraph*, November 9. Accessed August 25, 2017. http://www.telegraph.co.uk/news/worldnews/asia/china/11983156/Air-quality-plummets-as-heavy-smog-blankets-large-swaths-of-China.html.

Czlonkowska, A., and Kurkowska-Jastrzebska, I. (2011). Inflammation and gliosis in neurological diseases—Clinical implications. *J Neuroimmunol* **231**, 78–85.

Doty, R. L. (2008). The olfactory vector hypothesis of neurodegenerative disease: Is it viable? *Ann Neurol* **63**, 7–15.

Gao, H. (2016). Progress and perspectives on targeting nanoparticles for brain drug delivery. *Acta Pharm Sin B* **6**, 268–86.

Gotz, J., Schild, A., Hoerndli, F., and Pennanen, L. (2004). Amyloid-induced neurofibrillary tangle formation in Alzheimer's disease: Insight from transgenic mouse and tissue-culture models. *Int J Dev Neurosci* **22**, 453–65.

Hao, J., Zhao, J., Zhang, S., Tong, T., Zhuang, Q., Jin, K., Chen, W., and Tang, H. (2016). Fabrication of an ionic-sensitive in situ gel loaded with resveratrol nanosuspensions intended for direct nose-to-brain delivery. *Colloids Surf B Biointerfaces* **147**, 376–86.

Hauke, C., and Korr, H. (1993). RCA-I lectin histochemistry after trypsinisation enables the identification of microglial cells in thin paraffin sections of the mouse brain. *J Neurosci Methods* **50**, 273–77.

Heusinkveld, H. J., Wahle, T., Campbell, A., Westerink, R. H., Tran, L., Johnston, H., Stone, V., Cassee, F. R., and Schins, R. P. (2016). Neurodegenerative and neurological disorders by small inhaled particles. *Neurotoxicology* **56**, 94–106.

Hopkins, L. E., Patchin, E. S., Chiu, P. L., Brandenberger, C., Smiley-Jewell, S., and Pinkerton, K. E. (2014). Nose-to-brain transport of aerosolised quantum dots following acute exposure. *Nanotoxicology* **8**, 885–93.

Hughes, L. S., and Cass, G. R. (1998). Physical and chemical characterization of atmospheric ultrafine particles in the Los Angeles area. *Environ Sci Technol* **32**, 1153–61.

Jasinski, J., Pinkerton, K. E., Kennedy, I. M., and Leppert, V. J. (2006). Spatially resolved energy electron loss spectroscopy studies of iron oxide nanoparticles. *Microsc Microanal* **12**, 424–31.

Kim, Y. S., and Joh, T. H. (2006). Microglia, major player in the brain inflammation: Their roles in the pathogenesis of Parkinson's disease. *Exp Mol Med* **38**, 333–47.

Kovacs, T. (2004). Mechanisms of olfactory dysfunction in aging and neurodegenerative disorders. *Ageing Res Rev* **3**, 215–32.

Kreyling, W. G., Semmler, M., Erbe, F., Mayer, P., Takenaka, S., Schulz, H., Oberdorster, G., Ziesenis, A., et al (2002). Translocation of ultrafine insoluble iridium particles from lung epithelium to extrapulmonary organs is size dependent but very low. *J Toxicol Environ Health A* **65**, 1513–30.

Kumar, V., and Gill, K. D. (2009). Aluminium neurotoxicity: Neurobehavioural and oxidative aspects. *Arch Toxicol* **83**, 965–78.

Lawson, L. J., Perry, V. H., Dri, P., and Gordon, S. (1990). Heterogeneity in the distribution and morphology of microglia in the normal adult mouse brain. *Neuroscience* **39**, 151–70.

Linse, S., Cabaleiro-Lago, C., Xue, W. F., Lynch, I., Lindman, S., Thulin, E., Radford, S. E., and Dawson, K. A. (2007). Nucleation of protein fibrillation by nanoparticles. *Proc Natl Acad Sci USA* **104**, 8691–96.

Majde, J. A. (2010). Neuroinflammation resulting from covert brain invasion by common viruses—A potential role in local and global neurodegeneration. *Med Hypotheses* **75**, 204–13.

Mistry, A., Stolnik, S., and Illum, L. (2009). Nanoparticles for direct nose-to-brain delivery of drugs. *Int J Pharm* **379**, 146–57.

Mombaerts, P. (2006). Axonal wiring in the mouse olfactory system. *Annu Rev Cell Dev Biol* **22**, 713–37.

Muntimadugu, E., Dhommati, R., Jain, A., Challa, V. G., Shaheen, M., and Khan, W. (2016). Intranasal delivery of nanoparticle encapsulated tarenflurbil: A potential brain targeting strategy for Alzheimer's disease. *Eur J Pharm Sci* **92**, 224–34.

Ngo, M. A., Pinkerton, K. E., Freeland, S., Geller, M., Ham, W., Cliff, S., Hopkins, L. E., et al. (2010). Airborne particles in the San Joaquin Valley may affect human health. *Calif Agr* **64**, 12–16.

Oberdorster, G., Sharp, Z., Atudorei, V., Elder, A., Gelein, R., Kreyling, W., and Cox, C. (2004). Translocation of inhaled ultrafine particles to the brain. *Inhal Toxicol* **16**, 437–45.

Patchin, E. S., Anderson, D. S., Silva, R. M., Uyeminami, D. L., Scott, G. M., Guo, T., Van Winkle, L. S., and Pinkerton, K. E. (2016). Size-dependent deposition, translocation, and microglial activation of inhaled silver nanoparticles in the rodent nose and brain. *Environ Health Perspect* **124**, 1870–75.

Pinkerton, K. E., and Joad, J. P. (2006). Influence of air pollution on respiratory health during perinatal development. *Clin Exp Pharmacol Physiol* **33**, 269–72.

Pinkerton, K. E., Zhou, Y., Zhong, C., Smith, K. R., Teague, S. V., Kennedy, I. M., and Menache, M. G. (2008). Mechanisms of particulate matter toxicity in neonatal and young adult rat lungs. *Res Rep Health Eff Inst* **135**, 3–41; discussion 43–52.

Pott Godoy, M. C., Tarelli, R., Ferrari, C. C., Sarchi, M. I., and Pitossi, F. J. (2008). Central and systemic IL-1 exacerbates neurodegeneration and motor symptoms in a model of Parkinson's disease. *Brain* **131**, 1880–94.

Pui, D. Y. H., Chen, S. C., and Zuo, Z. (2014). PM$_{2.5}$ in China: Measurements, sources, visibility and health effects, and mitigation. *Particuology* **13**, 1–26.

Rao, D. B., Wong, B. A., McManus, B. E., McElveen, A. M., James, A. R., and Dorman, D. C. (2003). Inhaled iron, unlike manganese, is not transported to the rat brain via the olfactory pathway. *Toxicol Appl Pharmacol* **193**, 116–26.

Shaftel, S. S., Carlson, T. J., Olschowka, J. A., Kyrkanides, S., Matousek, S. B., and O'Banion, M. K. (2007). Chronic interleukin-1beta expression in mouse brain leads to leukocyte infiltration and neutrophil-independent blood brain barrier permeability without overt neurodegeneration. *J Neurosci* **27**, 9301–09.

Stence, N., Waite, M., and Dailey, M. E. (2001). Dynamics of microglial activation: A confocal time-lapse analysis in hippocampal slices. *Glia* **33**, 256–66.

Thornton, P., McColl, B. W., Cooper, L., Rothwell, N. J., and Allan, S. M. (2010). Interleukin-1 drives cerebrovascular inflammation via MAP kinase-independent pathways. *Curr Neurovasc Res* **7**, 330–40.

Wierzba-Bobrowicz, T., Lechowicz, W., and Kosno-Kruszewska, E. (1997). A morphometric evaluation of morphological types of microglia and astroglia in human fetal mesencephalon. *Folia Neuropathol* **35**, 29–35.

Yang, G. S., Teague, S., Pinkerton, K., and Kennedy, I. M. (2001). Synthesis of an ultrafine iron and soot aerosol for the evaluation of particle toxicity. *Aerosol Sci Technol* **35**, 759–66.

Zhong, C. Y., Zhou, Y. M., Smith, K. R., Kennedy, I. M., Chen, C. Y., Aust, A. E., and Pinkerton, K. E. (2010). Oxidative injury in the lungs of neonatal rats following short-term exposure to ultrafine iron and soot particles. *J Toxicol Environ Health A* **73**, 837–47.

Zhou, Y. M., Zhong, C. Y., Kennedy, I. M., Leppert, V. J., and Pinkerton, K. E. (2003). Oxidative stress and NFkappaB activation in the lungs of rats: A synergistic interaction between soot and iron particles. *Toxicol Appl Pharmacol* **190**, 157–69.

Zhou, Y. M., Zhong, C. Y., Kennedy, I. M., and Pinkerton, K. E. (2003). Pulmonary responses of acute exposure to ultrafine iron particles in healthy adult rats. *Environ Toxicol* **18**, 227–35.